ACS NANO

www.acsnano.org

ARTICLE

In Situ Imaging of Ferroelastic Domain Dynamics in $CsPbBr_3$ Perovskite Nanowires by Nanofocused Scanning X-ray Diffraction

Lucas A. B. Marçal, Eitan Oksenberg, Dmitry Dzhigaev, Susanna Hammarberg, Amnon Rothman, Alexander Björling, Eva Unger, Anders Mikkelsen, Ernesto Joselevich, and Jesper Wallentin*

Cite This: *ACS Nano* 2020, 14, 15973−15982

Read Online

ACCESS | Metrics & More | Article Recommendations | Supporting Information

ABSTRACT: **The interest in metal halide perovskites has grown as impressive results have been shown in solar cells, light emitting devices, and scintillators, but this class of materials have a complex crystal structure that is only partially understood. In particular, the dynamics of the nanoscale ferroelastic domains in metal halide perovskites remains difficult to study. An ideal *in situ* imaging method for ferroelastic domains requires a challenging combination of high spatial resolution and long penetration depth. Here, we demonstrate *in situ* temperature-dependent imaging of ferroelastic domains in a single nanowire of metal halide perovskite, $CsPbBr_3$. Scanning X-ray diffraction with a 60 nm beam was used to retrieve local structural properties for temperatures up to 140 °C. We observed a single Bragg peak at room temperature, but at 80 °C, four new Bragg peaks appeared, originating in different real-space domains. The domains were arranged in periodic stripes in the center and with a hatched pattern close to the edges. Reciprocal space mapping at 80 °C was used to quantify the local strain and lattice tilts, revealing the ferroelastic nature of the domains. The domains display a partial stability to further temperature changes. Our results show the dynamics of nanoscale ferroelastic domain formation within a single-crystal perovskite nanostructure, which is important both for the fundamental understanding of these materials and for the development of perovskite-based devices.**

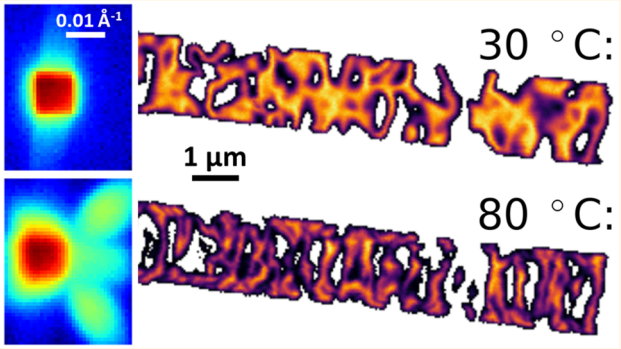

KEYWORDS: *perovskite, $CsPbBr_3$, ferroelasticity, nanowires, X-ray diffraction, domains*

During the past few years, metal halide perovskites (MHPs) have attracted the attention of the scientific community owing to their potential applications in photovoltaic and optoelectronic devices.[1−4] Many recent works have revealed the unique optical properties of these materials, and the development of devices based on MHPs has been swift.[5−9] MHPs exhibit several crystal phases with modest transition temperatures, which can be significantly affected by strain.[10] Among the MHPs, $CsPbBr_3$ exhibits good radiation stability, making it very promising for optoelectronic devices, including X-ray detectors.[11] Bulk $CsPbBr_3$ crystallizes in an orthorhombic structure (*Pbnm* with a = 8.20 Å, b = 8.25 Å, and c = 11.74 Å, and also commonly presented in the *Pnma* notation with a = 8.25 Å, b = 11.74 Å, and c = 8.20 Å) at room temperature (RT) and presents two structural phase transitions, one to tetragonal (*P4/mbm* with $a = b$ = 8.26 Å and c = 5.89 Å) at 88 °C and another one to cubic ($Pm\bar{3}m$ with $a = b = c$ = 5.56 Å) at 130 °C.[12,13] These phase-transition temperatures can be shifted by strain, especially in nanostructures.[6,13] The high photoluminescence quantum yield,[14] together with the ability to tune the emission wavelength by varying their length and width, has attracted ample interest for $CsPbBr_3$ nanowires.[15,16] However, although there are many studies on the growth and the optical and electronic properties of $CsPbBr_3$,[2,4,12,17−21] several basic questions regarding its structural properties are still open.

There is currently an intense debate on whether MHPs can present ferroelectricity[22] or just ferroelasticity.[23] Many non-MHP perovskites, such as $BaTiO_3$ and $PbTiO_3$, are well-known prototypical ferroelectrics;[24] others like $SrTiO_3$ (STO) can be

Received: September 3, 2020
Accepted: October 12, 2020
Published: October 19, 2020

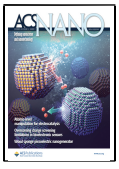

https://dx.doi.org/10.1021/acsnano.0c07426
ACS Nano 2020, 14, 15973−15982

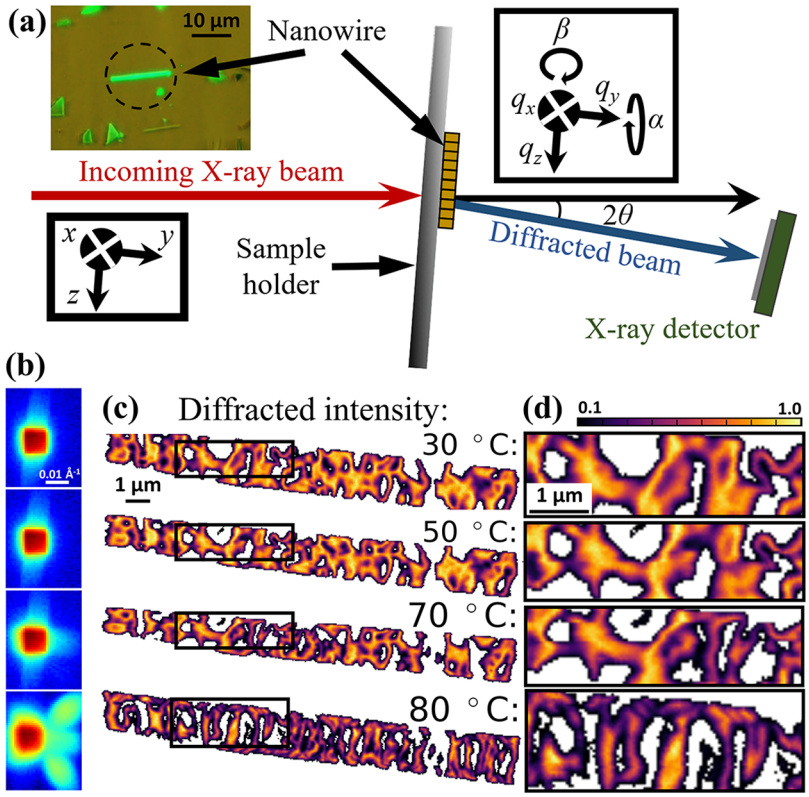

Figure 1. (a) Schematic representation of the experimental setup. The nanowire was rotated to the Bragg angle θ, and the X-ray detector was positioned at 2θ. The scattering vector components q_x, q_y, and q_z as well as lattice tilts α (rotation around q_y) and β (rotation around q_x) are defined in the inset. The main component of the scattering vector, q_z, is aligned with the nanowire axis. (b) X-ray detector frames showing the summed diffraction intensity along the nanowire with fixed θ at 30, 50, 70, and 80 °C, stacked from the top to bottom, respectively. At 80 °C, new diffraction peaks appear. (c) Real-space maps showing the local intensity of the Bragg peak at a single angle for different temperatures. A real-space map was acquired at each 10 °C step, of which we show a few here and the rest in the Supporting Information. The nanowire was heated from RT until 80 °C, when its crystalline structure underwent a significant change, forming a transversal stripe-like pattern. (d) A more detailed plot of the nanowire segments marked in (c) for each corresponding temperature. The step (pixel) size in (c) and (d) is 50 nm.

pushed toward a ferroelectric state,[25] while most perovskites occurring in the *Pbnm*/*Pnma* space group do not present ferroelectricity.[26] Recent literature, however, reports ferroelectricity in MHP thin films retrieved by scanning probe microscopy (SPM) methods such as piezoelectric force microscopy (PFM),[22,27] suggesting a polarization of the Pb atoms inside the unit cells. In ferroelastic materials, stress leads to the formation of domains with different crystal orientation.[28] It has been demonstrated that ferroelasticity can be a key to induce domain formation in different structures, including epitaxial tetragonal phase perovskites.[29,30] If two interfacing domains have different lattice spacings, the domains will generally tilt due to the lattice mismatch at the domain walls.[29−32] Likewise, ferroelastic domains could be formed in $CsPbBr_3$ single crystals induced by phase transitions.[33] Ferroelectric materials additionally exhibit electric polarization, which could affect the performance of MHP solar cells.[34−37] Studying ferroelectricity and ferroelasticity in MHPs is therefore important, both for applications and for a fundamental understanding of these materials.

MHPs have mainly been studied with optical techniques. For instance, phase transitions were indirectly inferred from microphotoluminescence (PL) with a modest spatial resolution,[5,21,38−40] while transmission electron microscopy (TEM) and SPM are atomic resolution methods commonly used to study ferroelectricity and ferroelasticity.[41,42] However, the latter two methods with such high spatial resolution and small fields of view have severe limitations. TEM requires invasive sample preparation, which also makes *in situ* studies of phase transitions challenging, and SPM can only probe the sample surface. In contrast, X-ray diffraction (XRD) can probe deep into samples that have been exposed to minimal preparation prior to the investigation, owing to the long absorption length of X-rays. Such characteristics make XRD ideal for studies of *in situ* processes, including temperature changes.[43] XRD is also very sensitive to lattice tilt and can be used to measure domain tilts with extremely high precision.[24,44−47] Traditionally, the real-space resolution of XRD has been poor, but the recent development in X-ray optics has made it possible to focus X-rays down to the nanoscale.[48,49] Scanning XRD using a nanofocused beam has enabled studies of single nanocrystals and nanoscale devices[50−52] as well as static imaging of ferroelectric domains.[53] However, dynamic *in situ* studies of ferroelastic or ferroelectric domains, which have a typical size of about 100 nm,[27,33] require a very small and bright X-ray focus. Here, we use the NanoMAX beamline,[48] situated at the first diffraction-limited storage ring MAX IV, to study the dynamics of ferroelastic domains in $CsPbBr_3$ nanowires during temperature variations, and demonstrate how scanning nano-XRD with a 60 nm beam size can be used for high-resolution *in situ* imaging of nanoscale ferroelastic domains within a single MHP nanowire.

https://dx.doi.org/10.1021/acsnano.0c07426
ACS Nano 2020, 14, 15973−15982

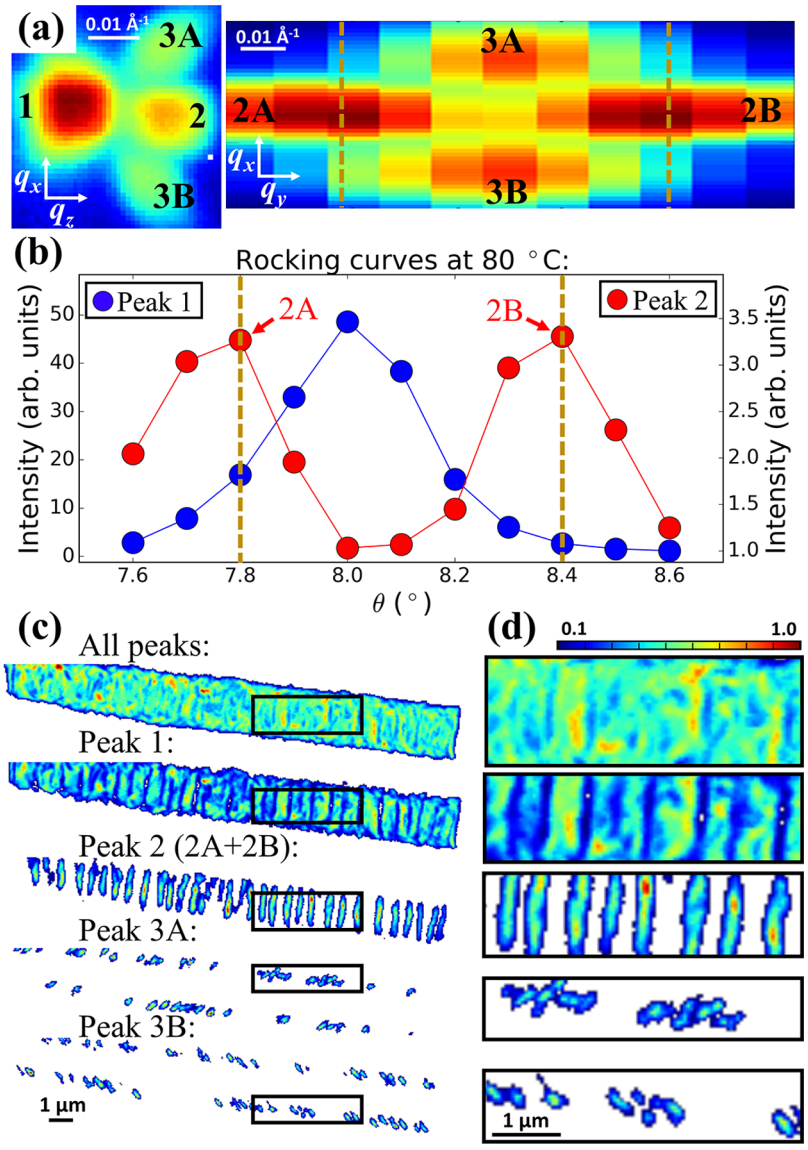

Figure 2. (a) The sum of the diffraction frames acquired by the X-ray detector for all real-space positions along the nanowire at 80 °C is depicted in the left panel, where q_z represents the main component of the scattering vector, Q. Peak 1 was observed at RT and is still present, while peaks 2, 3A, and 3B were observed at temperatures starting at 80 °C. The right panel shows a plane of the reciprocal space that slices the high temperature peaks (2, 3A, and 3B but not 1) for a specific q_z, evidencing that peak 2 is actually a dual peak appearing at two different tilts as well as the symmetry of the four new peaks. (b) Rocking curve for peaks 1 and 2, again evidencing how peak 2 is split around peak 1. The maxima positions marked on the rocking curve correspond to the marks on peaks 2A and 2B in (a). (c) Map of the integrated intensity along the nanowire for the total diffracted intensity (upper panel) as well as each individual peak. The map corresponding to peak 2 is associated with the sum of the diffracted intensity for peaks 2A and 2B. (d) Magnified plot of the areas marked in (c) for each corresponding peak. The pixel size in (c) and (d) is 50 nm.

RESULTS AND DISCUSSION

Nano-XRD of $CsPbBr_3$ Nanowires. $CsPbBr_3$ nanowires were grown on a fused silica glass substrate by thermal evaporation at elevated temperatures of >360 °C, analogous to previous reports.[17,54,55] Note that, for the experiment described here, nanowires were deposited on an amorphous substrate instead of a single-crystal sapphire[17] or mica.[54,55] We applied the scanning X-ray diffraction technique to study the crystalline structure of a single nanowire, 18 μm long, 2 μm wide and 450 nm thick, aligned parallel to the substrate surface. Without further preparation, the sample was mounted onto a heating stage and aligned in the X-ray focus. A schematic representation of the experimental setup can be seen in Figure 1a. A two-dimensional X-ray detector was positioned near the 2θ Bragg condition (17.158°) to collect the diffraction signal of the (004) reflection of the $CsPbBr_3$ orthorhombic (*Pbnm*) phase. By scanning the sample in the nanofocused beam, we obtained spatially resolved maps of the nanowire. Furthermore, with multiple projections acquired at slightly different θ values around the Bragg condition, *i.e.*, in a rocking curve, we could evaluate the three-dimensional reciprocal space, allowing for the reconstruction of the strain field and lattice tilt maps with high resolution.[52,56] The definition of the reciprocal space coordinates and the lattice tilts can be seen in the inset of Figure 1a. The nanowire's long axis was set along the *z*-axis, so q_z became the main scattering vector component. The α and β tilts are defined as the lattice rotations around q_y and q_x, respectively.

https://dx.doi.org/10.1021/acsnano.0c07426
ACS Nano 2020, 14, 15973−15982

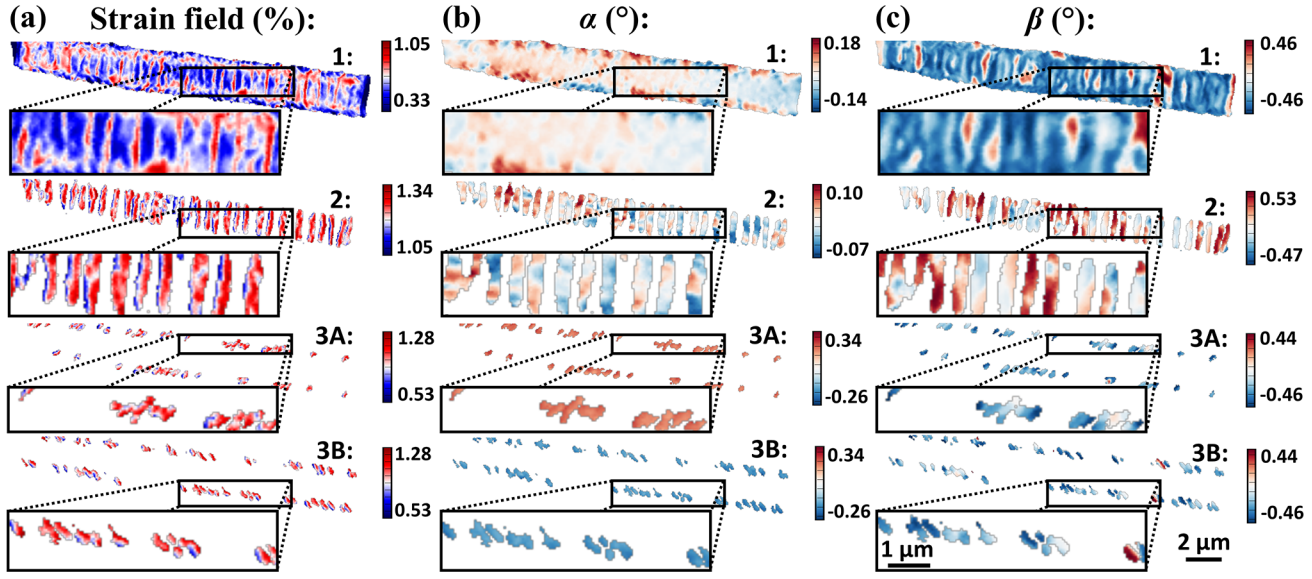

Figure 3. (a) Strain field and (b) α and (c) β maps of the nanowire for peaks 1 (upper panel), 2 (upper middle panel), 3A (bottom middle panel), and 3B (bottom panel). Insets show, with more details, the selected area for each corresponding map.

Temperature-Dependent Projection Maps. First, real-space maps were acquired at a fixed angle of incidence, corresponding to the maximum of the rocking curve, for a set of different temperatures, ranging from 30 to 80 °C. Each pixel in the maps represent the local intensity magnitude of the orthorhombic (004) Bragg peak. We tracked the nanowire while increasing the temperature until 80 °C, collecting a real-space map for every 10 °C step. The high flux of the nanofocus allowed a counting time of 10 ms per point, giving a total measurement time of approximately 10 min per image. From this data, we show selected temperatures in Figure 1, and the full set in Figure S2.

At RT, we observe a single Bragg peak and an intensity map with domains without any obvious order, as depicted in the upper panels of Figure 1b,c, respectively. The square shape of the peak in Figure 1b comes from the divergence of the Kirkpatrick-Baez (KB) mirror nanofocus. The intensity variations in the real-space maps, which are normalized, are an effect of local lattice tilts, and bright regions indicate that the crystal is better aligned at the Bragg condition for the given θ. In Figure S1, we present a full RT scanning XRD analysis of another nanowire. The nanowire shows intensity variations in the single projections, but all areas diffract at some angle; the total intensity is quite homogeneous. This result shows that the nanowires are crystalline with a single Bragg peak, but there are domains with slightly different orientations. The domains have a width on the order of a few hundred nanometers and remain nearly unchanged as the temperature increased up to 70 °C, as shown in the middle panels of Figure 1b,c.

At 80 °C, however, we observed a dramatic change: Three new diffraction peaks, nonexistent at low temperatures, clearly appear on the detector, as depicted in the bottom panel of Figure 1b. The new peaks, which will be named peaks 2, 3A, and 3B, in contrast with peak 1 that was already visible at RT, appear at a higher scattering angle 2θ, *i.e.*, smaller lattice spacing, as shown in the left panel of Figure 2a. Simultaneously, an ordered real-space domain pattern appeared. The center of the nanowire showed a striped pattern orthogonal to the long axis. In the region of about 300 nm into the nanowire, from both edges, the domains were oriented 45° relative to the edges. Such features can be seen in the bottom panel of Figure 1c. In Figure 1d, one can see part of the real-space projection maps selected in Figure 1c for each corresponding temperature in more detail.

Full Diffraction Analysis at 80 °C. With the temperature fixed at 80 °C, the nanowire was mapped for a set of θ angles around the Bragg condition, generating rocking curves that allowed for the reconstruction of the three-dimensional reciprocal space associated with different real-space positions. For each Bragg peak and for each real-space position, we can separately analyze the Bragg peak intensity (Figure 2). Furthermore, we can calculate the center of mass of the Bragg peak, from which the lattice strain and the two lattice tilts α and β can be determined (Figure 3). The integrated intensity maps are shown in Figure 2c for the sum of the diffraction peaks (upper panel). One can also see, in the subsequent panels of the same figure, the integrated and normalized diffracted intensity for peaks 1, 2, 3A, and 3B, separately.

From the full diffraction analysis, we find that peak 2 is in fact a double peak, which will be named 2A and 2B, with two different Bragg conditions, *i.e.*, two separate maxima values for θ in the rocking curve. The rocking curves, *i.e.*, the integrated intensity of all real-space positions as a function of θ, of peaks 1 and 2 are shown in Figure 2b. Peaks 2A and 2B have the same 2θ and lattice spacing but different lattice tilts. A different projection view of the reciprocal space, showing the q_x by q_y plane that slices the center of peaks 2A, 2B, 3A, and 3B but excludes peak 1, is depicted in the right panel of Figure 2a, revealing the symmetry of the four high temperature peaks. The measured angular distance for the center of mass of peaks 3A and 3B is 0.21(9)°, while peaks 2A and 2B are 0.64(5)° apart. Note that both splits are centered around peak 1.

The intensity maps integrated for all θ, depicted in Figure 2c, clearly show that the different Bragg peaks originate from different domains in the nanowire. The small area of the nanowire marked in Figure 2c is shown in more detail for the integrated intensity map corresponding to each peak in Figure 2d. The stripe-like pattern observed in the single projection map at 80 °C is associated with peaks 2A and 2B, and the

https://dx.doi.org/10.1021/acsnano.0c07426
ACS Nano 2020, 14, 15973−15982

hatched domains along the edges, with 45° rotation, are responsible for peaks 3A and 3B. When the diffraction coming from peaks 1 and 2 are isolated, a deep look into the corresponding integrated intensity maps reveals that such stripes consist of intercalated and complementary domains from those peaks. The peak 2 striped domains are about 250 nm thick and form a superlattice with an average center to center distance of 500 nm. Although peak 1 diffraction is still visible all over the nanowire, its low-intensity regions match the high-intensity regions of peak 2. Additionally, peaks 3A and 3B, which are associated with the edge domains, are also complementary and present an opposite orientation of their respective domains, as one can see in Figure 2c. Note that domains corresponding to peaks 3A and 3B can be found on both long edges but not the short ones.

Strain Maps. The full three-dimensional reciprocal space reconstruction, as a function of the real-space position, also allowed us to retrieve the spatially resolved strain field and lattice tilt maps along the nanowire. Figure 3a exhibits the distribution of the absolute strain field associated with peaks 1, 2, 3A, and 3B, stacked from top to bottom, respectively. The absolute strain values were calculated relative to the theoretical $CsPbBr_3$ orthorhombic phase bulk lattice parameters at 80 °C: a = 8.24 Å, b = 8.29 Å, and c = 11.80 Å.[12] An overall base tensile strain on the order of 0.5% is observed along the whole nanowire. It is expected for the nanostructure to exhibit some residual stress from the high temperature growth process.[57,58] The bulk $CsPbBr_3$ linear thermal expansion coefficient is found to be in the order of 1.2×10^{-4} K^{-4},[12] in contrast with the SiO_2, which is reported to be around 5.5×10^{-7} K^{-1} in the literature.[59] That could lead, from the 360 °C growth temperature, to a maximum strain in the order of $\epsilon_{thermal}$ = 3%.[60] Stripe-like domains are, again, visible for peaks 1 and 2 maps. A careful observation of the peak 2 strain field map shows internal strain gradients within the stripes, always in the same direction. Peaks 3A and 3B strain maps, although containing smaller domains only along the edges of the nanowire, follow the same overall strain gradient tendency seen for peak 2.

Lattice Tilts. Scanning nanofocused XRD is also very sensitive to local lattice tilts. In our measurement geometry, the tilt around the optical axis, α, leads to a split directly on the detector, which can be seen in Figure 2a for peaks 3A and 3B. The tilt around the rotation axis, β, gives a Bragg peak on the same position on the detector plane but at different θ, as seen in Figure 2a for peaks 2A and 2B. The α tilt maps of peaks 1 and 2, depicted in Figure 3b, show only small fluctuations on the order of 0.2°. In contrast, the β map for peak 2, shown in Figure 3c, exhibits different striped domains with distinct β tilts. Alternating maximum and minimum values, which range from −0.47° to +0.53°, indicate lattice undulations around q_x, *i.e.*, perpendicular to the substrate. Thus, each striped domain in the peak 2 map corresponds to either peak 2A or 2B. This effect is responsible for the appearance of two maxima on the peak 2 rocking curve, as plotted in Figure 2b, and also leads to the peak splitting seen by the q_x by q_y slice of the reciprocal space, depicted in the right panel of Figure 2a. There is no obvious pattern in the order of the 2A and 2B domains along the nanowire axis, and we observe an approximately equal number of domains of the two types. Conversely, the tilt maps for peaks 3A and 3B show that these domains have similar β tilt but present opposite α tilt, which leads to the peak splitting along q_x, seen in Figure 2a. The lattice tilt maps for the 3A and 3B domains are shown in the bottom panels of Figure 3b,c. Their colormap ranges were set to be the same for better comparison, and although they present α tilts ranging from −0.26° to 0.34°, the average difference between the two maps is about 0.22°, in agreement with Figure 2a.

To summarize, Figure 4 shows a schematic representation of nanowire domains at 80 °C. The gray background box

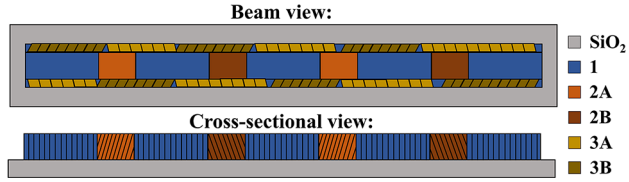

Figure 4. Nanowire sketch, showing the in-line X-ray beam perspective as well as an orthogonal cross-sectional view. Blue, light orange, dark orange, light yellow, and dark yellow colors correspond to peaks 1, 2A, 2B, 3A, and 3B, respectively, while the gray color was used to represent the SiO_2 substrate. 3A and 3B domain sizes as well as the representation of their plane inclinations with rotation around q_y are exaggerated for better visualization. Different domains associated with peaks 2A and 2B present plane inclinations with rotation around q_x, and thin lines indicate the lattice tilts (not to scale).

represents the SiO_2 substrate, while blue, light orange, dark orange, light yellow, and dark yellow colors are used to depict 1, 2A, 2B, 3A, and 3B domains, respectively. For better visualization, the lattice tilts of domains corresponding to peaks 2A, 2B, 3A, and 3B as well as the domain sizes of peaks 3A and 3B are exaggerated.

Stability of Domains. In order to investigate the stability and reversibility of the observed crystalline changes, we continued to ramp the temperature. First, the temperature was gradually decreased back to RT. The nanowire was tracked, and real-space map projections were, again, acquired every 10 °C as well as at 25 °C, repeating temperature steps used during heating. Some projection maps for temperatures ranging from 80 to 25 °C (RT) can be seen in Figure 5a as well as the sum of the diffraction frames acquired along the nanowire for each corresponding temperature (results from all measured temperatures can be found in Figure S5). It was notable that the high temperature diffraction peaks observed at 80 °C did not abruptly vanish at 70 °C, indicating hysteresis in the process. Peak 2, associated with the vertical stripe-like pattern, did not immediately disappear, as one could expect, but gradually vanished during the cooling cycle. In fact, part of the peak 2 intensity was still visible at 50 °C, gradually overlapping with peak 1. Peaks 3A and 3B, originating from the hatched pattern along the nanowire edges as well as part of the striped pattern on the real-space maps, remained until 25 °C, although they were weaker than at 80 °C. This result demonstrates a partial preservation of the high temperature crystalline organization.

Next, we increased the temperature of the nanowire directly to 80 °C and then in steps to 140 °C, again performing a real-space map acquisition for every 10 °C step (results from all measured temperatures can be found in Figure S6). One can see in Figure 5b real-space map projections and the corresponding detector images for different temperatures: 80, 100, 120, and 140 °C. Note that the measurement at 80 °C is a repeat after the cycling to RT. For higher temperatures, the domain shapes changed, becoming generally smaller and less

https://dx.doi.org/10.1021/acsnano.0c07426
ACS Nano 2020, 14, 15973−15982

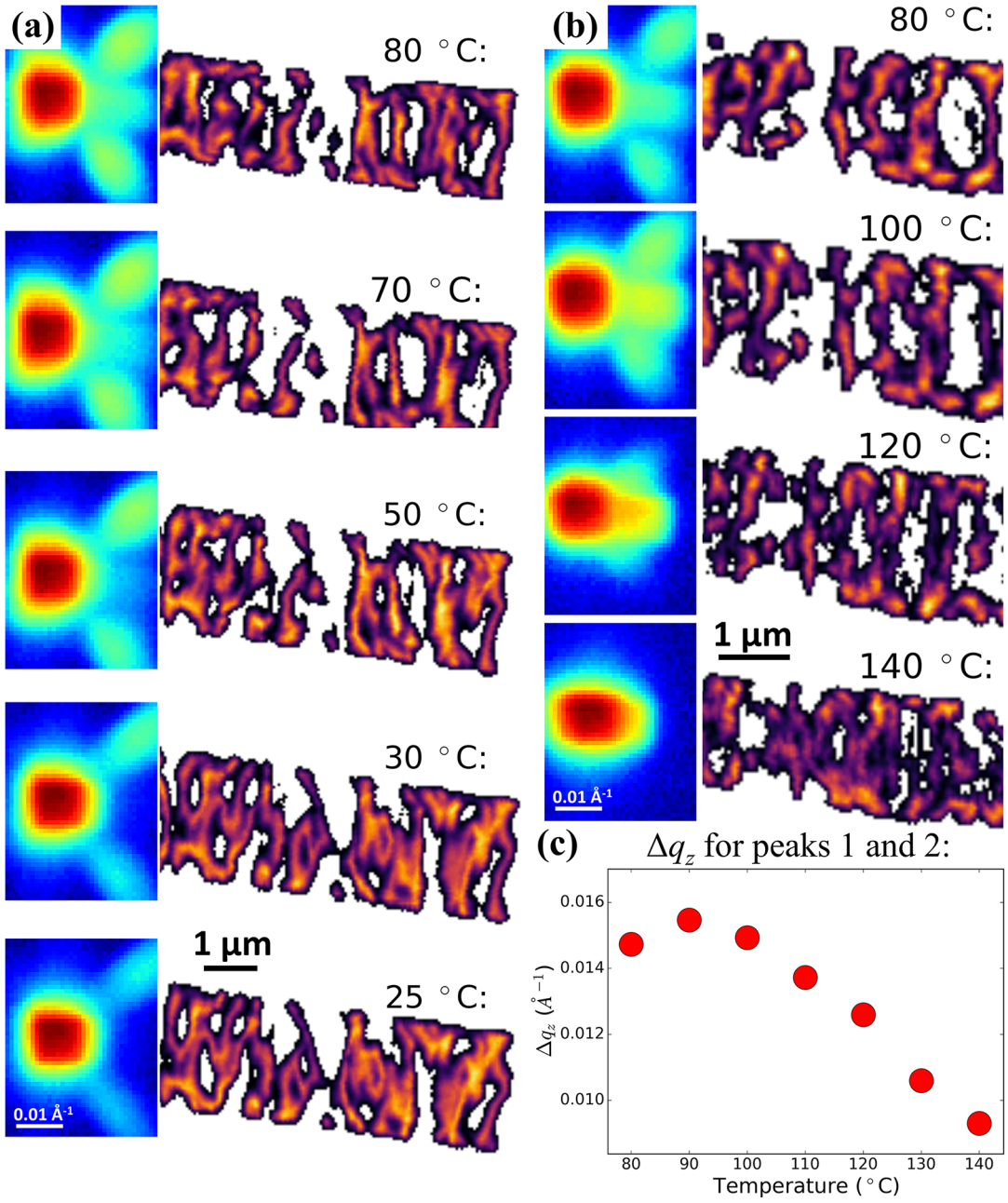

Figure 5. (a) Sum of the diffraction frames collected along the nanowire as well as part of the real-space map projections for temperatures below 80 °C acquired in the cooling process, showing that the nanowire partially preserves the structure created at 80 °C. The nanowire was mapped for every 10 °C step as well as at 25 °C (RT). (b) Diffraction frames and part of the real-space map projections acquired at higher temperatures, evidencing the extinction of the stripe-like pattern. The nanowire was, again, mapped after each 10 °C step, and the ones corresponding to 80, 100, 120, and 140 °C are shown. Note that the 80 °C map shown here was acquired after the low-temperature cycling. The real-space maps shown in (a) and (b) do not correspond to the same region. (c) Peaks 1 and 2 Δq_z plot for temperatures ranging from 80 to 140 °C.

ordered, while all peaks gradually merged into a single Bragg peak. Figure 5c plots the Δq_z split between peaks 1 and 2 at temperatures ranging from 80 to 140 °C. A clear systematic decrease in the peak splitting indicates the possibility of a gradual second phase transition, which has been reported in different scenarios for $CsPbBr_3$ nanocrystals.[13,61] After this process, we also cooled the nanowire down again to repeat the diffraction mappings at 75 °C and RT, obtaining results similar to the previous cooling cycle. The real-space maps and diffraction frames for these temperatures can be found in Figure S7. Bulk $CsPbBr_3$ changes its crystal structure from tetragonal to cubic at 130 °C. Our observations indeed indicate that the whole nanowire might present the same crystalline structure at high temperatures, and the center of the mass of the summed diffraction frames at 140 °C is in agreement with the cubic (002) reflection. The observed domains here would then correspond to different local lattice tilts, similar to the initial RT state and the reference nanowire depicted in Figure S1. However, note that we have neither a full rocking curve nor measurements from multiple reflections at high temperature, which prevents firm conclusions.

https://dx.doi.org/10.1021/acsnano.0c07426
ACS Nano 2020, 14, 15973−15982

Local Crystal Structure. An important question is which crystal phases and reflections are associated with the different domains. To determine the possible reflections associated with each peak, it is important to notice that the scattering vector is parallel with the nanowire axis, so all crystal planes that we observe must be nearly orthogonal to this axis. On average, the difference in the length of the scattering vectors measured for peak 1, when compared with peaks 2 and 3, is $\Delta Q = 0.0179$ Å^{-1}, which corresponds to a relative difference in lattice spacing of about 0.9%. One possible interpretation is that the nanowire undergoes a phase transition at 80 °C from orthorhombic to tetragonal. In this case, the domain pattern is due to striped intercalating tetragonal domains with different unit cell orientations, one with its *c*-axis oriented along the nanowire (peak 1) and the second one with the *c*-axis parallel to the domain walls[29] (peaks 2 and 3). This is similar to the striped *a*/*c*/*a* domains observed in tetragonal non-MHP perovskites.[29,30] It is known from the literature that the tetragonal bulk $CsPbBr_3$ lattice constants at 80 °C are approximately $a = b = 8.26$ Å and $c = 5.89$ Å.[12,13] Such a hypothesis would mean that the larger domains, associated with peak 1, correspond to tetragonal (002) and have the *c*-axis along the nanowire axis. In contrast, the shorter domains then have the *c*-axis orthogonal to the nanowire axis, forming the four possible tetragonal (220)-type reflections corresponding to the peaks 2A, 2B, 3A, and 3B. A theoretical split of $\Delta Q = 0.0154$ Å^{-1} is expected for these reflections, which is 14% lower than what, on average, we observe for peaks 1 and 2. A second hypothesis is that the part of the nanowire associated with peak 1 preserves its RT crystalline structure and that this is the orthorhombic (004) reflection, while peaks 2A, 2B, 3A, and 3B again correspond to the four possible tetragonal (220)-type reflections with different tilts with respect to the domain walls. In this case, the theoretical $\Delta Q = 0.0189$ Å^{-1} is only 6% higher than what we observe.[12,13] We also made measurements at $2\theta = 8.579°$, corresponding to half of the initial measured Bragg angle (Figure S3). At this condition, two Bragg peaks were still visible, which is consistent with both hypotheses. Phase coexistence has been recently reported on $MAPbI_3$ nanowires studied by temperature-dependent PL[5] and TEM,[61] and as described in the Supporting Information Section 4, such a mixed crystal structure would only require small changes in the rotation of the perovskite octahedrons. Similarities on the overall atomic position indicate that low energy is expected for the transitions associated with both discussed scenarios.

Ferroelastic Domain Tilts. In order to understand the observed presence of tilts in peaks 2 and 3, we have to consider the lattice mismatch. Although the atomic arrangements are similar, the unit cell lengths at the domain walls are not exactly the same. Lattice mismatched domain walls can induce ferroelasticity, which in turn can lead to tilted domains.[29] To calculate the expected tilts, the distance $(a_{TET}^2 + b_{TET}^2)^{1/2} = 11.68$ Å or $(a_{ORT}^2 + b_{ORT}^2)^{1/2} = 11.69$ Å for peak 1 representing the tetragonal (002) and orthorhombic (004) reflections, respectively, will be matched with the larger $2c_{TET} = 11.78$ Å. For an infinite, unstrained layer in the simplest model, this would lead to a tilt of $\omega = 1 - [(a_{TET}^2 + b_{TET}^2)^{1/2}/2c_{TET}] = 0.48°$ for the first scenario and $\omega = 1 - [(a_{ORT}^2 + b_{ORT}^2)^{1/2}/2c_{TET}] = 0.44°$ for the second case, relative to the reference.[30] Although the measured tilts are on the same order of magnitude, our results are more complicated. On average, the 2A and 2B peaks are tilted ±0.32°, while the 3A and 3B peaks present ±0.11° tilts. It is important to keep in mind that the nanowire is not infinitely thick, as assumed for the theoretical model, and this will reduce the tilt.[30] Also, the strain can affect the mismatch at the interface, and we know that the nanowire is tensile strained in the *z*-direction. We do not know the strain in the *x*- and *y*-directions, but it is reasonable to assume that they are different, leading to different amounts of tilt for peaks 2 and 3.

CONCLUSIONS

We have presented high-resolution *in situ* imaging of the complex dynamics of ferroelastic domains in a single $CsPbBr_3$ crystal during temperature variation. Studies of MHP phase transition peculiarities and ferroelastic domain dynamics are essential to understand their structural properties, which in turn affect their electrical and optical properties. These insights could only be achieved with a method that has both nanoscale spatial resolution and allows for *in situ* measurements of complete samples. A dramatic change in the crystalline structure was observed at 80 °C, close to the orthorhombic to tetragonal transition temperature for bulk $CsPbBr_3$, with the appearance of four new Bragg peaks that we assign to tetragonal (220)-type reflections. The combination of high resolution and large field of view also revealed a highly organized pattern, with domains presenting an ordered stripe-like domain pattern in the center and a hatched pattern near the edges. Clearly, the surface at the edge affects the domain formation, an effect that would be more significant in smaller nanostructures than the nanowire presented here. We find that the tetragonal peaks show lattice tilts consistent with ferroelastic domains, with plane inclinations being responsible for the appearance of four tetragonal (220)-type reflections. Furthermore, we find that the domains formed at 80 °C are partially stable to further cycling to lower and higher temperatures. Future experiments could investigate the effects of controlled mechanical stress on the local crystal structure.[62]

Methodologically, our results demonstrate how scanning XRD with a nanofocused beam can be used for *in situ* studies of ferroelastic domain dynamics. The high coherent flux of the first diffraction limited storage ring MAX IV allows fast measurements with high resolution in real-space, strain, and lattice tilt. The long absorption length of X-rays makes it possible to perform *in situ* nanofocused scanning XRD in air of a minimally prepared sample and would also allow investigations of complete devices or samples in a controlled environment. The method presented here should be applicable to a wide range of materials, including non-MHP ferroelectric and ferroelastic materials.

METHODS

$CsPbBr_3$ Horizontal Nanowire Synthesis. The noncatalyzed growth was carried out in a three-zone horizontal-tube furnace. The quartz tube reactor was purged with a N_2 (99.999%, Gordon Gas) and H_2 (99.99995%, Parker Dominic Hunter H_2-generator) 7:1 mixture and maintained at 300 mbar with a constant 400 sccm flow of the N_2/H_2 mixture during the growth process. For the growth process, 150–180 μm thick, UV-grade, fused silica glass (Laser Optex Inc.) substrates were used. CsBr and $PbBr_2$ powders (both purchased from Sigma-Aldrich) were mixed in a 1:2 molar ratio and heated at 390 °C for 20 min in the same N_2/H_2 atmosphere to generate the precursor. During the growth process the precursor was held at 550 °C in the first heating zone of the furnace, while the silica glass samples were placed downstream in the second heating zone and held at 360 °C.

https://dx.doi.org/10.1021/acsnano.0c07426
ACS Nano 2020, 14, 15973–15982

After a 15 min growth period, the furnace was moved away, and the source and sample could be rapidly cooled to room temperature.

Temperature-Dependent Nanofocused Scanning X-ray Diffraction. The X-ray diffraction experiment was performed upon transmission geometry using a nanofocused beam at the NanoMAX beamline at MAX IV Laboratory in Lund, Sweden. The beam was focused to 64 × 61 nm^2 (vertical × horizontal) spot size using a set of KB mirrors. The energy of the beam was fixed at 14.087 keV (wavelength 0.8801 Å), during the nanodiffraction experiments with an incident flux of 10^9 photons/second. The Bragg angle position was calibrated using a Si foil. The sample was mounted inside a heating chamber, built by Leiden Probe Microscopy, specially designed for synchrotron experiments, which allowed for temperature variation. The heater controller was integrated to the beamline control system, so it was possible to change the sample temperature without the need to enter the hutch. The chamber was attached to a fast *xyz* scanning piezoelectric stage with a lateral stroke of 100 μm and a resolution of 10 nm. Gold markers on the sample allowed for the first alignment of the coarse motors using an in-line microscope. The diffracted beam was recorded using a Merlin photon-counting detector with 515 × 515 pixels of 55 μm^2 pixel size positioned at 400 mm away from the sample. A Pilatus 100K detector, collecting the transmitted beam, was used to verify the alignment of the nanowire during the scanning diffraction measurements. Real-space misalignments of the nanowire were later compensated during data analysis. A realignment of the piezoelectric motor position was also necessary after each temperature step, since we could note a shift due to thermal expansion of about 2–3 μm for every 10 °C variation. Simultaneously combining high-speed continuous motion of the *xyz* scanning piezoelectric stage and high frequency data acquisition, we were able to obtain two-dimensional diffraction maps and then reconstruct real-space maps of the sample for different Bragg angles.

Data Availability. All data sets generated and analyzed during the current study are available from the corresponding author on reasonable request.

Code Availability. All custom codes used during the current study are available from the corresponding author on reasonable request.

ASSOCIATED CONTENT

Supporting Information

The Supporting Information is available free of charge at https://pubs.acs.org/doi/10.1021/acsnano.0c07426.

> Nano-XRD on reference nanowire, crystalline structure change, low angle measurements, crystal phases, cooling down cycle, temperatures above 80 °C, and second cooling cycle (PDF)

AUTHOR INFORMATION

Corresponding Author

Jesper Wallentin − *Synchrotron Radiation Research and NanoLund, Lund University, 22100 Lund, Sweden;* orcid.org/0000-0001-5909-0483; Email: jesper.wallentin@sljus.lu.se

Authors

Lucas A. B. Marçal − *Synchrotron Radiation Research and NanoLund, Lund University, 22100 Lund, Sweden*

Eitan Oksenberg − *Center for Nanophotonics, AMOLF, 1098 XG Amsterdam, Netherlands; Department of Materials and Interfaces, Weizmann Institute of Science, Rehovot 76100, Israel*

Dmitry Dzhigaev − *Synchrotron Radiation Research and NanoLund, Lund University, 22100 Lund, Sweden;* orcid.org/0000-0001-8398-9480

Susanna Hammarberg − *Synchrotron Radiation Research and NanoLund, Lund University, 22100 Lund, Sweden*

Amnon Rothman − *Department of Materials and Interfaces, Weizmann Institute of Science, Rehovot 76100, Israel;* orcid.org/0000-0002-7095-8279

Alexander Björling − *MAX IV Laboratory, Lund University, 22100 Lund, Sweden*

Eva Unger − *Helmholtz-Zentrum Berlin für Materialien und Energie GmbH, Young Investigator Group Hybrid Materials Formation and Scaling, 12489 Berlin, Germany; Division of Chemical Physics and NanoLund, Lund University, 22100 Lund, Sweden;* orcid.org/0000-0002-3343-867X

Anders Mikkelsen − *Synchrotron Radiation Research and NanoLund, Lund University, 22100 Lund, Sweden*

Ernesto Joselevich − *Department of Materials and Interfaces, Weizmann Institute of Science, Rehovot 76100, Israel;* orcid.org/0000-0002-9919-0734

Complete contact information is available at: https://pubs.acs.org/10.1021/acsnano.0c07426

Author Contributions

L.A.B.M., E.U. and J.W. planned the research. L.A.B.M. and J.W. wrote the manuscript. The sample synthesis was performed by E.O., A.R., and E.J. The heater was designed by A.M. Temperature-dependent XRD measurements were performed by L.A.B.M., D.D., S.H., A.B., and J.W. Data analysis was performed by L.A.B.M and J.W. All authors discussed the data and contributed to the manuscript.

Notes

The authors declare no competing financial interest.

ACKNOWLEDGMENTS

This project has received funding from the European Research Council (ERC) under the European Union's Horizon 2020 research and innovation programme (grant agreement No. 801847). This research was also funded by the Olle Engkvist foundation, NanoLund, and Marie Sklodowska Curie Actions Cofund, Project INCA 600398. We acknowledge MAX IV Laboratory for time on Beamline NanoMAX under Proposal 20190248. Research conducted at MAX IV, a Swedish national user facility, is supported by the Swedish Research council under contract 2018-07152, the Swedish Governmental Agency for Innovation Systems under contract 2018-04969, and Formas under contract 2019-02496. E.J. acknowledges support from the European Research Council (ERC) PoC Grant (No. 838702) and the Israel Science Foundation (No. 2444/19). E.J. holds the Drake Family Professorial Chair of Nanotechnology.

REFERENCES

(1) Zhang, W.; Eperon, G. E.; Snaith, H. J. Metal Halide Perovskites for Energy Applications. *Nature Energy* **2016**, *1* (6), 16048.

(2) Kovalenko, M. V.; Protesescu, L.; Bodnarchuk, M. I. Properties and Potential Optoelectronic Applications of Lead Halide Perovskite Nanocrystals. *Science* **2017**, *358* (6364), 745–750.

(3) Doherty, T. A. S.; Winchester, A. J.; Macpherson, S.; Johnstone, D. N.; Pareek, V.; Tennyson, E. M.; Kosar, S.; Kosasih, F. U.; Anaya, M.; Abdi-Jalebi, M.; Andaji-Garmaroudi, Z.; Wong, E. L.; Madeo, J.; Chiang, Y. H.; Park, J. S.; Jung, Y. K.; Petoukhoff, C. E.; Divitini, G.; Man, M. K. L.; Ducati, C.; et al. Performance-Limiting Nanoscale Trap Clusters at Grain Junctions in Halide Perovskites. *Nature* **2020**, *580* (7803), 360–366.

(4) Oksenberg, E.; Sanders, E.; Popovitz-Biro, R.; Houben, L.; Joselevich, E. Surface-Guided CsPbBr3 Perovskite Nanowires on Flat

and Faceted Sapphire with Size-Dependent Photoluminescence and Fast Photoconductive Response. *Nano Lett.* **2018**, *18* (1), 424−433.
(5) Dobrovolsky, A.; Merdasa, A.; Unger, E. L.; Yartsev, A.; Scheblykin, I. G. Defect-Induced Local Variation of Crystal Phase Transition Temperature in Metal-Halide Perovskites. *Nat. Commun.* **2017**, *8* (1), 34.
(6) Kirschner, M. S.; Diroll, B. T.; Guo, P.; Harvey, S. M.; Helweh, W.; Flanders, N. C.; Brumberg, A.; Watkins, N. E.; Leonard, A. A.; Evans, A. M.; Wasielewski, M. R.; Dichtel, W. R.; Zhang, X.; Chen, L. X.; Schaller, R. D. Photoinduced, Reversible Phase Transitions in All-Inorganic Perovskite Nanocrystals. *Nat. Commun.* **2019**, *10* (1), 504.
(7) Whitfield, P. S.; Herron, N.; Guise, W. E.; Page, K.; Cheng, Y. Q.; Milas, I.; Crawford, M. K. Structures, Phase Transitions and Tricritical Behavior of the Hybrid Perovskite Methyl Ammonium Lead Iodide. *Sci. Rep.* **2016**, *6* (1), 35685.
(8) Filip, M. R.; Eperon, G. E.; Snaith, H. J.; Giustino, F. Steric Engineering of Metal-Halide Perovskites with Tunable Optical Band Gaps. *Nat. Commun.* **2014**, *5*, 5757.
(9) Amat, A.; Mosconi, E.; Ronca, E.; Quarti, C.; Umari, P.; Nazeeruddin, M. K.; Gratzel, M.; De Angelis, F. Cation-Induced Band-Gap Tuning in Organohalide Perovskites: Interplay of Spin-Orbit Coupling and Octahedra Tilting. *Nano Lett.* **2014**, *14* (6), 3608−16.
(10) Steele, J. A.; Jin, H.; Dovgaliuk, I.; Berger, R. F.; Braeckevelt, T.; Yuan, H.; Martin, C.; Solano, E.; Lejaeghere, K.; Rogge, S. M. J.; Notebaert, C.; Vandezande, W.; Janssen, K. P. F.; Goderis, B.; Debroye, E.; Wang, Y.-K.; Dong, Y.; Ma, D.; Saidaminov, M.; Tan, H.; et al. Thermal Unequilibrium of Strained Black CsPbI3 Thin Films. *Science* **2019**, *365*, 679.
(11) Zhang, H.; Wang, F.; Lu, Y.; Sun, Q.; Xu, Y.; Zhang, B.-B.; Jie, W.; Kanatzidis, M. G. High-Sensitivity X-Ray Detectors Based on Solution-Grown Caesium Lead Bromide Single Crystals. *J. Mater. Chem. C* **2020**, *8* (4), 1248−1256.
(12) Stoumpos, C. C.; Malliakas, C. D.; Peters, J. A.; Liu, Z.; Sebastian, M.; Im, J.; Chasapis, T. C.; Wibowo, A. C.; Chung, D. Y.; Freeman, A. J.; Wessels, B. W.; Kanatzidis, M. G. Crystal Growth of the Perovskite Semiconductor CsPbBr3: A New Material for High-Energy Radiation Detection. *Cryst. Growth Des.* **2013**, *13* (7), 2722−2727.
(13) Cottingham, P.; Brutchey, R. L. Depressed Phase Transitions and Thermally Persistent Local Distortions in CsPbBr3 Quantum Dots. *Chem. Mater.* **2018**, *30* (19), 6711−6716.
(14) Park, S.; Cho, H.; Choi, W.; Zou, H.; Jeon, D. Y. Correlation of near-Unity Quantum Yields with Photogenerated Excitons in X-Type Ligand Passivated CsPbBr3 Perovskite Quantum Dots. *Nanoscale Advances* **2019**, *1* (8), 2828−2834.
(15) Schlaus, A. P.; Spencer, M. S.; Miyata, K.; Liu, F.; Wang, X.; Datta, I.; Lipson, M.; Pan, A.; Zhu, X. Y. How Lasing Happens in CsPbBr3 Perovskite Nanowires. *Nat. Commun.* **2019**, *10* (1), 265.
(16) Liu, Y.; Guo, M.; Dong, S.; Jiao, X.; Wang, T.; Chen, D. Room Temperature Colloidal Synthesis of CsPbBr3 Nanowires with Tunable Length, Width and Composition. *J. Mater. Chem. C* **2018**, *6* (29), 7797−7802.
(17) Oksenberg, E.; Merdasa, A.; Houben, L.; Kaplan-Ashiri, I.; Rothman, A.; Scheblykin, I. G.; Unger, E. L.; Joselevich, E. Large Lattice Distortions and Size-Dependent Bandgap Modulation in Epitaxial Halide Perovskite Nanowires. *Nat. Commun.* **2020**, *11* (1), 489.
(18) Shamsi, J.; Urban, A. S.; Imran, M.; De Trizio, L.; Manna, L. Metal Halide Perovskite Nanocrystals: Synthesis, Post-Synthesis Modifications, and Their Optical Properties. *Chem. Rev.* **2019**, *119* (5), 3296−3348.
(19) Sebastian, M.; Peters, J. A.; Stoumpos, C. C.; Im, J.; Kostina, S. S.; Liu, Z.; Kanatzidis, M. G.; Freeman, A. J.; Wessels, B. W. Excitonic Emissions and Above-Band-Gap Luminescence in the Single-Crystal Perovskite Semiconductors CsPbBr3 and CsPbCl3. *Phys. Rev. B: Condens. Matter Mater. Phys.* **2015**, *92* (23), 235210.
(20) Zhang, M.; Zheng, Z.; Fu, Q.; Chen, Z.; He, J.; Zhang, S.; Yan, L.; Hu, Y.; Luo, W. Growth and Characterization of All-Inorganic Lead Halide Perovskite Semiconductor CsPbBr3 Single Crystals. *CrystEngComm* **2017**, *19* (45), 6797−6803.
(21) Gibson, N. A.; Koscher, B. A.; Alivisatos, A. P.; Leone, S. R. Excitation Intensity Dependence of Photoluminescence Blinking in CsPbBr3 Perovskite Nanocrystals. *J. Phys. Chem. C* **2018**, *122* (22), 12106−12113.
(22) Rohm, H.; Leonhard, T.; Schulz, A. D.; Wagner, S.; Hoffmann, M. J.; Colsmann, A. Ferroelectric Properties of Perovskite Thin Films and Their Implications for Solar Energy Conversion. *Adv. Mater.* **2019**, *31* (26), 1806661.
(23) Strelcov, E.; Dong, Q.; Li, T.; Chae, J.; Shao, Y.; Deng, Y.; Gruverman, A.; Huang, J.; Centrone, A. CH3NH3PbI3 Perovskites: Ferroelasticity Revealed. *Science Advances* **2017**, *3*, e1602165.
(24) Potnis, P. R.; Tsou, N. T.; Huber, J. E. A Review of Domain Modelling and Domain Imaging Techniques in Ferroelectric Crystals. *Materials* **2011**, *4* (2), 417−447.
(25) Kang, K. T.; Seo, H. I.; Kwon, O.; Lee, K.; Bae, J.-S.; Chu, M.-W.; Chae, S. C.; Kim, Y.; Choi, W. S. Ferroelectricity in SrTiO3 Epitaxial Thin Films *via* Sr-Vacancy-Induced Tetragonality. *Appl. Surf. Sci.* **2020**, *499*, 143930.
(26) Benedek, N. A.; Fennie, C. J. Why Are There So Few Perovskite Ferroelectrics? *J. Phys. Chem. C* **2013**, *117* (26), 13339−13349.
(27) Lee, J. C. T.; Damodaran, A. R.; Ramesh, R.; Martin, L. W.; Abbamonte, P. X-Ray Diffraction Studies of Stripelike Ferroelectric Domains in Thin Films of BiFeO3. *Phys. Rev. B: Condens. Matter Mater. Phys.* **2014**, *89*, 214104.
(28) Salje, E. K. H. Ferroelastic Materials. *Annu. Rev. Mater. Res.* **2012**, *42* (1), 265−283.
(29) Foster, C. M.; Pompe, W.; Daykin, A. C.; Speck, J. S. Relative Coherency Strain and Phase Transformation History in Epitaxial Ferroelectric Thin Films. *J. Appl. Phys.* **1996**, *79* (3), 1405−1415.
(30) Speck, J. S.; Daykin, A. C.; Seifert, A.; Romanov, A. E.; Pompe, W. Domain Configurations due to Multiple Misfit Relaxation Mechanisms in Epitaxial Ferroelectric Thin Films. III. Interfacial Defects and Domain Misorientations. *J. Appl. Phys.* **1995**, *78* (3), 1696−1706.
(31) Pompe, W.; Gong, X.; Suo, Z.; Speck, J. S. Elastic Energy Release Due to Domain Formation in the Strained Epitaxy of Ferroelectric and Ferroelastic Films. *J. Appl. Phys.* **1993**, *74* (10), 6012−6019.
(32) Romanov, A. E.; Pompe, W.; Speck, J. S. Theory of Microstructure and Mechanics of the···a1/a2/a1/a2··· Domain Pattern in Epitaxial Ferroelectric and Ferroelastic Films. *J. Appl. Phys.* **1996**, *79* (8), 4037−4049.
(33) Zhang, X.; Wang, F.; Zhang, B.-B.; Zha, G.; Jie, W. Ferroelastic Domains in a CsPbBr3 Single Crystal and Their Phase Transition Characteristics: An *in Situ* TEM Study. *Cryst. Growth Des.* **2020**, *20*, 4585−4592.
(34) Gorfman, S.; Simons, H.; Iamsasri, T.; Prasertpalichat, S.; Cann, D. P.; Choe, H.; Pietsch, U.; Watier, Y.; Jones, J. L. Simultaneous Resonant X-Ray Diffraction Measurement of Polarization Inversion and Lattice Strain in Polycrystalline Ferroelectrics. *Sci. Rep.* **2016**, *6*, 20829.
(35) Grigoriev, A.; Do, D. H.; Kim, D. M.; Eom, C. B.; Adams, B.; Dufresne, E. M.; Evans, P. G. Nanosecond Domain Wall Dynamics in Ferroelectric Pb(Zr, Ti)O(3) Thin Films. *Phys. Rev. Lett.* **2006**, *96* (18), 187601.
(36) Zhao, Y. Q.; Ma, Q. R.; Liu, B.; Yu, Z. L.; Cai, M. Q. Pressure-Induced Strong Ferroelectric Polarization in Tetra-Phase Perovskite CsPbBr3. *Phys. Chem. Chem. Phys.* **2018**, *20* (21), 14718−14724.
(37) Xiao, X.; Li, W.; Fang, Y.; Liu, Y.; Shao, Y.; Yang, S.; Zhao, J.; Dai, X.; Zia, R.; Huang, J. Benign Ferroelastic Twin Boundaries in Halide Perovskites for Charge Carrier Transport and Recombination. *Nat. Commun.* **2020**, *11* (1), 2215.
(38) Lee, S. M.; Moon, C. J.; Lim, H.; Lee, Y.; Choi, M. Y.; Bang, J. Temperature-Dependent Photoluminescence of Cesium Lead Halide Perovskite Quantum Dots: Splitting of the Photoluminescence Peaks

https://dx.doi.org/10.1021/acsnano.0c07426
ACS Nano 2020, 14, 15973−15982

of CsPbBr3 and CsPb(Br/I)3 Quantum Dots at Low Temperature. *J. Phys. Chem. C* **2017**, *121* (46), 26054−26062.
(39) Li, X.; Luo, Y.; Holt, M. V.; Cai, Z.; Fenning, D. P. Residual Nanoscale Strain in Cesium Lead Bromide Perovskite Reduces Stability and Shifts Local Luminescence. *Chem. Mater.* **2019**, *31* (8), 2778−2785.
(40) Tian, Y.; Merdasa, A.; Unger, E.; Abdellah, M.; Zheng, K.; McKibbin, S.; Mikkelsen, A.; Pullerits, T.; Yartsev, A.; Sundstrom, V.; Scheblykin, I. G. Enhanced Organo-Metal Halide Perovskite Photoluminescence from Nanosized Defect-Free Crystallites and Emitting Sites. *J. Phys. Chem. Lett.* **2015**, *6* (20), 4171−7.
(41) Li, W.; Zhang, Z.; Bithell, E. G.; Batsanov, A. S.; Barton, P. T.; Saines, P. J.; Jain, P.; Howard, C. J.; Carpenter, M. A.; Cheetham, A. K. Ferroelasticity in a Metal−Organic Framework Perovskite; towards a New Class of Multiferroics. *Acta Mater.* **2013**, *61* (13), 4928−4938.
(42) Li, X.; Chen, S.; Liu, P. F.; Zhang, Y.; Chen, Y.; Wang, H. L.; Yuan, H.; Feng, S. Evidence for Ferroelectricity of All-Inorganic Perovskite CsPbBr3 Quantum Dots. *J. Am. Chem. Soc.* **2020**, *142* (7), 3316−3320.
(43) Gorfman, S.; Keeble, D. S.; Bombardi, A.; Thomas, P. A. Topology and Temperature Dependence of the Diffuse X-Ray Scattering in Na0.5Bi0.5TiO3 Ferroelectric Single Crystals. *J. Appl. Crystallogr.* **2015**, *48*, 1543−1550.
(44) Schmidbauer, M.; Hanke, M.; Kwasniewski, A.; Braun, D.; von Helden, L.; Feldt, C.; Leake, S. J.; Schwarzkopf, J. Scanning X-Ray Nanodiffraction from Ferroelectric Domains in Strained K0.75Na0.25NbO3 Epitaxial Films Grown on (110) TbScO3. *J. Appl. Crystallogr.* **2017**, *50* (2), 519−524.
(45) Hruszkewycz, S. O.; Zhang, Q.; Holt, M. V.; Highland, M. J.; Evans, P. G.; Fuoss, P. H. Structural Sensitivity of X-Ray Bragg Projection Ptychography to Domain Patterns in Epitaxial Thin Films. *Phys. Rev. A: At., Mol., Opt. Phys.* **2016**, *94* (4), No. 043803.
(46) Bertolotti, F.; Protesescu, L.; Kovalenko, M. V.; Yakunin, S.; Cervellino, A.; Billinge, S. J. L.; Terban, M. W.; Pedersen, J. S.; Masciocchi, N.; Guagliardi, A. Coherent Nanotwins and Dynamic Disorder in Cesium Lead Halide Perovskite Nanocrystals. *ACS Nano* **2017**, *11* (4), 3819−3831.
(47) Bertolotti, F.; Nedelcu, G.; Vivani, A.; Cervellino, A.; Masciocchi, N.; Guagliardi, A.; Kovalenko, M. V. Crystal Structure, Morphology, and Surface Termination of Cyan-Emissive, Six-Monolayers-Thick CsPbBr3 Nanoplatelets from X-Ray Total Scattering. *ACS Nano* **2019**, *13* (12), 14294−14307.
(48) Bjorling, A.; Kalbfleisch, S.; Kahnt, M.; Sala, S.; Parfeniukas, K.; Vogt, U.; Carbone, G.; Johansson, U. Ptychographic Characterization of a Coherent Nanofocused X-Ray Beam. *Opt. Express* **2020**, *28* (4), 5069−5076.
(49) Chayanun, L.; Hammarberg, S.; Dierks, H.; Otnes, G.; Bjorling, A.; Borgstrom, M. T.; Wallentin, J. Combining Nanofocused X-Rays with Electrical Measurements at the NanoMAX Beamline. *Crystals* **2019**, *9* (8), 432.
(50) Chayanun, L.; Otnes, G.; Troian, A.; Hammarberg, S.; Salomon, D.; Borgstrom, M. T.; Wallentin, J. Nanoscale Mapping of Carrier Collection in Single Nanowire Solar Cells Using X-Ray Beam Induced Current. *J. Synchrotron Radiat.* **2019**, *26* (1), 102−108.
(51) Troian, A.; Otnes, G.; Zeng, X.; Chayanun, L.; Dagytė, V.; Hammarberg, S.; Salomon, D.; Timm, R.; Mikkelsen, A.; Borgström, M. T.; Wallentin, J. Nanobeam X-Ray Fluorescence Dopant Mapping Reveals Dynamics of *in Situ* Zn-Doping in Nanowires. *Nano Lett.* **2018**, *18* (10), 6461−6468.
(52) Marçal, L. A. B.; Richard, M. I.; Magalhães-Paniago, R.; Cavallo, F.; Lagally, M. G.; Schmidt, O. G.; Schülli, T. Ü.; Deneke, C.; Malachias, A. Direct Evidence of Strain Transfer for InAs Island Growth on Compliant Si Substrates. *Appl. Phys. Lett.* **2015**, *106* (15), 151905.
(53) Hruszkewycz, S. O.; Highland, M. J.; Holt, M. V.; Kim, D.; Folkman, C. M.; Thompson, C.; Tripathi, A.; Stephenson, G. B.; Hong, S.; Fuoss, P. H. Imaging Local Polarization in Ferroelectric Thin Films by Coherent X-Ray Bragg Projection Ptychography. *Phys. Rev. Lett.* **2013**, *110* (17), 177601.
(54) Wang, Y.; Sun, X.; Shivanna, R.; Yang, Y.; Chen, Z.; Guo, Y.; Wang, G. C.; Wertz, E.; Deschler, F.; Cai, Z.; Zhou, H.; Lu, T. M.; Shi, J. Photon Transport in One-Dimensional Incommensurately Epitaxial CsPbX3 Arrays. *Nano Lett.* **2016**, *16* (12), 7974−7981.
(55) Chen, J.; Fu, Y.; Samad, L.; Dang, L.; Zhao, Y.; Shen, S.; Guo, L.; Jin, S. Vapor-Phase Epitaxial Growth of Aligned Nanowire Networks of Cesium Lead Halide Perovskites (CsPbX3, X = Cl, Br, I). *Nano Lett.* **2017**, *17* (1), 460−466.
(56) Wallentin, J.; Jacobsson, D.; Osterhoff, M.; Borgstrom, M. T.; Salditt, T. Bending and Twisting Lattice Tilt in Strained Core-Shell Nanowires Revealed by Nanofocused X-Ray Diffraction. *Nano Lett.* **2017**, *17* (7), 4143−4150.
(57) Hetnarski, R. B. *Encyclopedia of Thermal Stresses*; Springer Netherlands: Dordrecht, 2014.
(58) Abadias, G.; Chason, E.; Keckes, J.; Sebastiani, M.; Thompson, G. B.; Barthel, E.; Doll, G. L.; Murray, C. E.; Stoessel, C. H.; Martinu, L. Review Article: Stress in Thin Films and Coatings: Current Status, Challenges, and Prospects. *J. Vac. Sci. Technol., A* **2018**, *36* (2), No. 020801.
(59) Tada, H.; Kumpel, A. E.; Lathrop, R. E.; Slanina, J. B.; Nieva, P.; Zavracky, P.; Miaoulis, I. N.; Wong, P. Y. Thermal Expansion Coefficient of Polycrystalline Silicon and Silicon Dioxide Thin Films at High Temperatures. *J. Appl. Phys.* **2000**, *87* (9), 4189−4193.
(60) Moridi, A.; Ruan, H.; Zhang, L. C.; Liu, M. Residual Stresses in Thin Film Systems: Effects of Lattice Mismatch, Thermal Mismatch and Interface Dislocations. *Int. J. Solids Struct.* **2013**, *50* (22−23), 3562−3569.
(61) Whitcher, T. J.; Gomes, L. C.; Zhao, D.; Bosman, M.; Chi, X.; Wang, Y.; Carvalho, A.; Hui, H. K.; Chang, Q.; Breese, M. B. H.; Castro Neto, A. H.; Wee, A. T. S.; Sun, H. D.; Chia, E. E. M.; Rusydi, A. Dual Phases of Crystalline and Electronic Structures in the Nanocrystalline Perovskite CsPbBr3. *NPG Asia Mater.* **2019**, *11* (1), 70.
(62) Leclere, C.; Cornelius, T. W.; Ren, Z.; Davydok, A.; Micha, J.-S.; Robach, O.; Richter, G.; Belliard, L.; Thomas, O. *In Situ* Bending of an Au Nanowire Monitored by Micro Laue Diffraction. *J. Appl. Crystallogr.* **2015**, *48*, 291−296.

https://dx.doi.org/10.1021/acsnano.0c07426
ACS Nano 2020, 14, 15973−15982